Timescales of bubble coalescence, outgassing, and foam collapse in decompressed rhyolitic melts

Caroline Martel *, Giada Iacono-Marziano

Université d'Orléans, CNRS/INSU, ISTO, BRGM, UMR 7327, 45071 Orléans, France

ARTICLE INFO

Article history:
Received 4 February 2014
Received in revised form 1 December 2014
Accepted 4 December 2014
Available online 7 January 2015
Editor: T. Elliott

Keywords:
decompression
coalescence
outgassing
foam collapse
permeability
rhyolitic melt

ABSTRACT

The timescale of degassing and outgassing in hydrous rhyolitic melts is investigated in a wide range of conditions by means of decompression experiments. The evolution of vesicularity, bubble diameter, and number density is characterized as a function of time either of decompression or spent at final pressure, in order to determine the effect of final pressure, temperature, syn- versus post-decompression degassing, melt composition, and microlites, on the timescale of bubble growth, coalescence, and outgassing.

The result suggests that different bubble evolution and degassing–outgassing timescale corresponding to explosive and effusive eruption regimes can be cast in bulk viscosity (melt + bubbles; η_{bulk}) versus decompression time (rather than path) space. The η_{bulk}–time relationship defines three domains of (i) bubble nucleation and growth, restricted to short durations and high η_{bulk} ($<\sim$0.03 h for η_{bulk} $\sim 10^{5-6}$ Pa s), (ii) equilibrium degassing with coalescence increasing from negligible (permeability $> 10^{-13}$ m^2) to extensive (permeability $\sim 10^{-11-12}$ m^2), and (iii) outgassing, restricted to long durations and low η_{bulk} ($>\sim$10 h for $\eta_{bulk} < 10^6$ Pa s; permeability $>10^{-10}$ m^2) that eventually leads to foam collapse.

These findings are applied to the case studies of Mt Pelée and Mt Pinatubo to infer the transition from pumice to dense pyroclasts in volcanic eruptions and the possibility of evolving from an explosive Plinian eruption to an effusive dome-growth event by giving the vesicular magma enough time to outgas and collapse (i.e. hundreds to tens of hours for η_{bulk} $\sim 10^5$ to 10^4 Pa s, respectively). We also show the drastic effect of microlites on re-arranging preexistent bubbles and potentially triggering a late nucleation event.

1. Introduction

Explosive volcanic eruptions have aroused great interest in understanding the mechanisms of degassing and the transitions between explosive and effusive eruptions of silicic magmas. When silicic magmas rise from depth to the Earth surface, gas solubility decreases and the oversaturated melt exsolves gases as bubbles that grow by gas diffusion and vapor expansion. Either bubbles remain isolated and trapped in the melt or they coalesce to form connected gas channels that promote gas escape and eventually foam collapse (Eichelberger et al., 1986). In the case of isolated bubbles, the magma may be overpressurized with gas and trigger a highly explosive eruption, whereas in the case of bubble interconnection, the magma may outgas and erupt effusively. Thus, investigating the whole degassing process (i.e. the dynamics of bubble nucleation, growth, coalescence, and evacuation) is crucial to our understanding of the transitions in eruptive styles. Since the pioneering study of Sparks (1978), degassing and bubble dynamics in silicic melts have been extensively investigated through experiments (e.g. Navon et al., 1998; Gardner et al., 1999; Larsen and Gardner, 2000; Martel and Bureau, 2001; Gondé et al., 2011) and numerical models (e.g. Toramaru, 1989, 1995; Barclay et al., 1995; Proussevitch and Sahagian, 1996, 1998).

Many parameters control the degassing of ascending magmas, such as melt composition, volatile content, temperature, and decompression rate. As a result, it is not always clear which of those parameters dominates bubble evolution and degassing. Many studies have focused on the effect of decompression rate on bubble nucleation in silicic melts (e.g. Mangan and Sisson, 2000; Mourtada-Bonnefoi and Laporte, 2004; Toramaru, 2006; Hamada et al., 2010), whereas others aimed at defining the parameters controlling bubble growth (e.g. Sparks, 1978; Barclay et al., 1995; Lyakhovsky et al., 1996; Proussevitch and Sahagian, 1998; Gardner et al., 1999; Liu and Zhang, 2000). Investigations have also been conducted on the factors promoting bubble interconnectivity, such as coalescence, permeability development, and foam collapse in

* Corresponding author. Tel.: +33 2 38 25 52 52; fax: +33 2 38 49 44 76.
E-mail address: caroline.martel@cnrs-orleans.fr (C. Martel).

rhyolitic magmas (e.g. Eichelberger et al., 1986; Westrich and Eichelberger, 1994; Klug and Cashman, 1994, 1996; Blower et al., 2002; Larsen et al., 2004; Burgisser and Gardner, 2005; Gardner, 2007; Degruyter et al., 2010; Castro et al., 2012a; Takeuchi et al., 2009). Up to now, bubble nucleation and growth are the most understood processes, thanks to combined natural, experimental, and numerical studies. The conditions of bubble coalescence and foam collapse are so far more poorly understood, although directly linked to the ability of the magma to erupt explosively or effusively.

In order to assess the respective roles of parameters such as melt composition, pressure, and temperature, on the mechanisms and timescales of bubble coalescence and outgassing, we conducted experiments of decompression-induced degassing in hydrated rhyolitic or rhyolite-analogue melts. The choice of the composition is dictated by the fact that rhyolitic melts commonly represent the chemical composition of the matrix that embeds phenocrysts in andesites, dacites or rhyolites. Decompression simulates magma ascent in a volcanic conduit. These new experiments complete a set of previously published decompression experiments that were mainly designed for crystallization studies (Martel and Schmidt, 2003; Martel, 2012; Mollard et al., 2012). The new data are acquired using the same (or very close) hydrated rhyolitic melts as starting material, were decompressed in similar devices, were processed similarly, so that both the new and previous data cover a large range of conditions important for examining the degassing–outgassing processes. We determined the time-evolution of vesicularity, bubble diameter and number density, critical to the characterization of bubble growth, coalescence, and foam collapse as a function of time and bulk viscosity (which depends on melt composition, temperature, H_2O content, and bubble content). By focusing on long-timescale processes in decompressing rhyolite melts, we offer new insights into bubble coalescence and outgassing, which are probably the most elusive stages of the vesiculation process.

2. Experimental and analytical methods

2.1. Composition of the starting materials

Three glass compositions have been used as starting material: two rhyolites (RHY and SHILL) and a haplotonalite (HTN). RHY is the composition of the rhyolitic matrix glass of the andesite of Mt Pelée, Martinique (RHY in wt%: 75.7 SiO_2, 13.1 Al_2O_3, 2.4 CaO, 3.6 Na_2O, 1.9 K_2O, 2.5 FeO, 0.4 MgO, 0.1 MnO, and 0.3 TiO_2). RHY glass preparation is described in Martel (2012). SHILL is the composition of the rhyolitic matrix glass of the andesite of Soufriere Hills, Montserrat (SHILL in wt%: 75.0 SiO_2, 13.6 Al_2O_3, 2.5 CaO, 4.3 Na_2O, 1.7 K_2O, 2.0 FeO, 0.4 MgO, 0.2 MnO, and 0.3 TiO_2). SHILL glass preparation is described in Martel and Schmidt (2003). RHY and SHILL are so similar in composition that we considered them directly comparable. HTN is a 4-component simplified composition of a rhyolite (HTN in wt%: 78.7 SiO_2, 14.1 Al_2O_3, 1.8 CaO, 5.4 Na_2O). HTN glass preparation is described in Mollard et al. (2012). With respect to RHY and SHILL, HTN allows testing any compositional differences due to either an enrichment in SiO_2 (~3 wt%) or the absence of ferromagnesian oxides.

2.2. Experimental methods

The decompression experiments were all performed in externally-heated pressure vessels at temperatures between 850 and 875 °C from an initial pressure (P_i) of 200 or 150 MPa to final pressures (P_f) varying between 10 and 60 MPa. The series were decompressed either (i) quasi-continuously following decompression rates from 0.2 to 50 000 MPa/h or (ii) rapidly (57–1200 MPa/h) to P_f followed by a dwell time ranging from 4 to 672 h at P_f. The samples were quenched at P_f within ~1–2 s. For ease, the continuous decompressions not followed by a dwell at P_f were referred as to "syn-decompression" degassing and the rapid decompressions followed by a dwell at P_f were referred as to "post-decompression" degassing although a part of the degassing may have started during decompression. A detailed guide to the experimental procedures is given in the *Supplementary Information_A*, the different decompression series are presented in Table 1, and the experimental conditions are given in Table 2.

Table 1
Summary of the decompression series and their experimental conditions.

Series name	Starting material[a]	T (°C)	P_i (MPa)	P_f (MPa)	Degassing style[b]
850SYN50	RHY	850	200	50	SYN
850SYN30	RHY	850	200	30	SYN
850SYN10	RHY	850	200	10	SYN
850POST50	RHY	850	200	50	POST
850POST30	RHY	850	200	30	POST
850POST10	RHY	850	200	10	POST
875POST50	RHY	875	200	50	POST
875POST50HTN	HTN	875	200	50	POST
860SYN50	SHILL	860	150	50	SYN

[a] RHY for Mt Pelée rhyolite, SHILL for Soufriere Hills rhyolite, and HTN for haplotonalite (compositions given in text).
[b] SYN for syn-decompression degassing and POST for post-decompression degassing, as defined in text.

2.3. Textural analysis of the bubbles

Either half the sample-bearing capsule or the biggest pieces of the sample were mounted in epoxy resin for analysis. Bubbles were investigated using images from optical or scanning electron microscopes (SEM). The images were processed using GIMP open-source software (GNU Image Manipulation Program) and converted into binary images for the determination of the porosity (Φ) and bubble size distribution using the SPO software [fabric analysis using the intercept method developed by Launeau and Robin (1996) and Launeau and Cruden (1998)]. SEM or optical images, together with their corresponding binary images, are shown as time-series in *Supplementary Information_B*. An example of one decompression series is shown in Fig. 1. Our wish was to keep the samples as pristine as possible to avoid introducing bias in the degassing interpretation, but we sometimes had to manually separate touching bubbles where polishing plucking was suspected (e.g. sample D7 in *Supplementary Information_Be*). We checked that this procedure of manual bubble separation did not significantly impact bubble number density (no shift greater than one log unit) or bubble size distribution. For the H_2O-saturated samples, some bubbles were trapped in the melt during the hydration procedure. In the samples decompressed in less than ~0.1 h, these pre-decompression bubbles were several times larger than the decompression-induced ones and we easily ruled them out from the analyses (e.g. sample SH11 from the 860SYN50 series in *Supplementary Information_Bh*). However, they were no more distinguishable from the decompression-induced bubbles for longer times and were thus counted together. Nevertheless, these initial bubbles likely have a negligible effect on the whole degassing process because they were always in proportion below 1 vol% and in number density several orders of magnitude lower than the decompression-induced bubbles (from measurements carried out on the samples held at P_i and not subjected to decompression).

From the binary images of the samples, we determined the following parameters:

- Φ, the porosity defined as the area ratio of bubbles to bubbles + glass (+ crystals, if any);

Table 2
Experimental and analytical conditions.

Sample	Series[a]	Experimental conditions[b]			Bubble analysis[c]			Crystals
		ΔP_{time} (h)	ΔP_{rate} (MPa/h)	Time at P_f (h)	Φ (vol%)	D_{max} (μm)	$\log N_v$ (m^{-3})	ψ (vol%)
RHY								
VP2	850SYN50	0.017	9000	0	5(4)	50(10)	13.75	7
VP3	850SYN50	0.25	600	0	24(4)	80(15)	13.88	9
VP14	850SYN50	2	75	0	27(4)	80(20)	14.32	9
VP5	850SYN50	10	15	0	23(4)	130(15)	13.05	11
VP8	850SYN50	48	3.12	0	29(4)	200(15)	12.64	13
VP6	850SYN50	120	1.25	0	27(4)	200(40)	12.20	13
VP10	850POST50	0.25	600	96	29(4)	250(40)	13.20	17
VP18	850SYN10	12.5	14.8	0	66(5)	500(100)	12.70	~10
VP13	850SYN10	151.2	1.22	0	61(5)	500(100)	12.42	12
D9	850SYN/POST30	1.5	113	0	47(5)	130(30)	13.51	8
D3	850SYN30	3	56.7	0	49(5)^{3D}	130(30)	13.71	10
D26	850SYN30	24	7.1	0	56(5)*	320(60)	12.14	1
D27	850SYN30	48	3.5	0	51(5)*	320(60)	12.00	6
D25	850SYN30	72	2.36	0	57(5)*	320(30)	12.08	10
D7	850SYN/POST10	1.5	127	0	80(5)*	500(100)	12.93	0
D33	850SYN10	72	2.6	0	60(5)*^{3D}	510(100)	11.96	10
D38	850SYN10	144	1.32	0	63(5)	500(100)	12.21	15
D4	850SYN10	333	0.57	0	51(5)	200(100)	12.67	22
D35	850SYN10	960	0.20	0	58(5)*^{3D}	320(60)	10.65	16
D20	850POST50	1.5	93	4	26(3)	200(60)	12.97	0
D2	850POST30	3	56.7	96	55(5)	320(60)	12.40	23
D8	850POST30	1.5	113	102	58(5)	320(80)	13.18	20
D34	850POST30	0.25	680	48	51(5)*^{3D}	400(80)	12.08	23
D39	850POST30	1.5	113	24	54(5)*^{3D}	400(60)	12.11	6
D12	850POST10	1.5	127	95	62(5)	500(100)	11.51	27
D6	850POST10	1.5	127	329	43(5)	400(100)	13.02	>30
A1	875POST50	0.125	1200	0	37(5)	127(22)	13.24	0
A2	875POST50	0.125	1200	6	5(2)	51(11)	12.96	0
A3	875POST50	0.125	1200	24	2(2)	80(17)	11.66	0
A4	875POST50	0.125	1200	48	3(2)	80(18)	11.07	1
A5	875POST50	0.125	1200	72	9(2)	75(10)	11.22	1
A6	875POST50	0.125	1200	96	9(2)	75(10)	11.16	1
A7	875POST50	0.125	1200	168	5(2)	75(10)	11.16	3
A8	875POST50	0.125	1200	408	1(1)	50(10)	11.09	6
A9	875POST50	0.125	1200	672	3(2)	50(10)	11.07	12
HTN								
HTN1	875POST50HTN	0.125	1200	0	44(5)	200(40)	12.66	0
HTN2	875POST50HTN	0.125	1200	6	42(5)	320(70)	11.48	0.1
HTN3	875POST50HTN	0.125	1200	16	28(4)	320(70)	11.91	0.4
HTN4	875POST50HTN	0.125	1200	24	4(2)	80(15)	12.32	1
HTN5	875POST50HTN	0.125	1200	48	3(2)	80(15)	11.65	4
SHILL (from Martel and Schmidt, 2003)								
SH16	860SYN50	0.002	50 000	0	17(2)	6(1)	15.68	0
SH12	860SYN50	0.004	25 000	0	30(4)*	10(1)	15.30	2
SH11	860SYN50	0.02	5000	0	30(4)*	25(2)	14.93	10
SH1	860SYN50	0.2	500	0	35(4)*	100(15)	13.13	7
SH4	860SYN50	10	10	0	32(4)*	250(15)	12.05	8
SH3	860SYN50	120	0.8	0	35(4)*	400(50)	11.70	18
SH5	860SYN50	360	0.3	0	30(4)*	400(50)	11.44	16

[a] Decompression series as defined in Table 1 (the first and last number of the series gives T and P_f, respectively; SYN and POST means syn- or post-decompression degassing, respectively).

[b] ΔP_{time} and ΔP_{rate} are the decompression duration and decompression rate, respectively.

[c] Φ is the porosity measured by SEM or XRCT (^{3D}), with (*) denoting the presence of pre-decompression bubbles; D_{max} is the maximum diameter of the bubbles; the numbers in brackets give the error resulting from repetitive analyses of at least three images of the same sample; N_v is bubble number density calculated after Higgins (2000); ψ is the percentage of microlites recalculated on a bubble-free basis.

- D_{max}, the maximum diameter of the continuous diameter distribution of discs having areas equivalent to the real bubble areas (thus not considering large diameters that are disconnected/isolated from the histogram of the whole population). Because the bubble population is assumed to be mono-modal and shows mostly sub-spherical sections, the maximum diameter represents the equator section and is assumed to the true diameter of the three-dimensional bubbles;
- N_v, the stereological bubble number density determined from the 2D bubble diameter population using CSD Corrections software (Higgins, 2000).

Five samples amongst the largest were imaged using XRay-computed tomograph (XRCT; Phoenix Nanotom 180, ISTO, Orléans, France), in order to compare 2D with 3D porosities and to model permeability. Processing any single image from the whole XRCT image stack suggests that 2D Φ have a maximum variability of ±5 vol% around the reconstructed 3D value. The samples processed both by XRCT and image analysis on polished sections (2D) also show Φ variations of only ±5 vol%. The bubble measurements are reported in Table 2. The permeability (κ) of four of these samples was modeled using Palabos open-source software [a computational-fluid-dynamics (CFD) solver based on the lattice

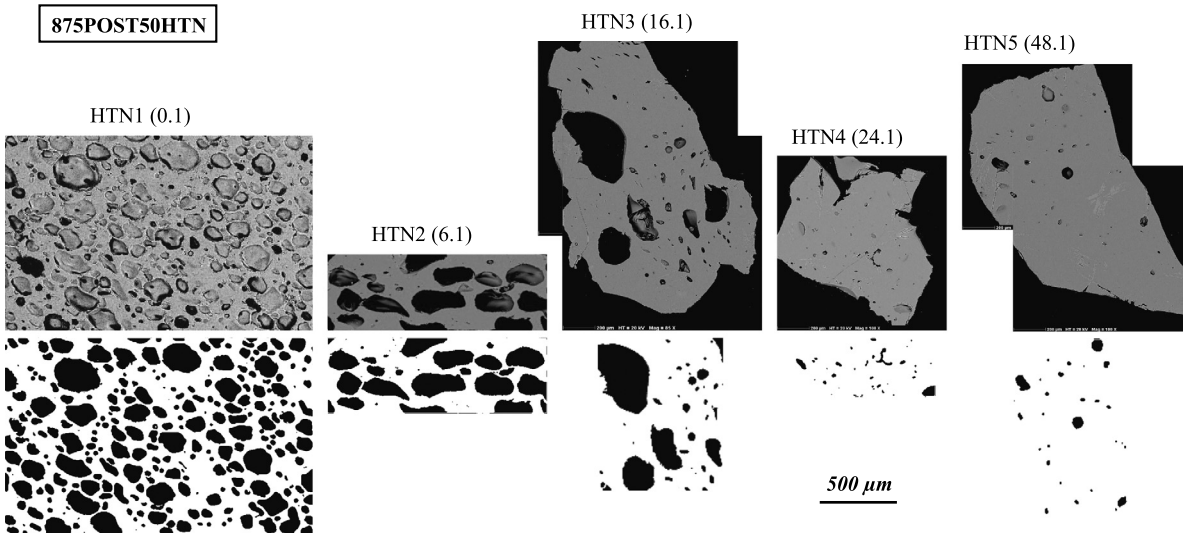

Fig. 1. SEM and associated binary images for 875POST50HTN for which the HTN starting material was rapidly decompressed at 875 °C from 200 to 50 MPa. From left to right, time spent at P_f increases from 0.1 to 48 h (duration given in hour in bracket next to sample number as in Table 2); scale bar of 500 µm for all images.

Table 3
Permeability calculation.

Series[a]	Sample[b]	Φ[c] (vol%)	$\log \kappa$[d] (m^2)
850SYN10	D33	60(5)	−10.2
850POST30	D39	54(5)	−11.5
850POST30	D34	51(5)	−12.1
850SYN30	D3	49(5)	−13.2

[a] Series as in Table 1.
[b] Sample number as in Table 2.
[c] Sample porosity as in Table 2.
[d] Permeability (average over the X–Y–Z directions) calculated after Palabos open-source software using XRCT images.

Boltzmann method] modified after Degruyter et al. (2010). This model requires the input of reconstructed XRCT images, thresholded for porosity, and simulates a downwards fluid injection from the top face of a cubic sample (whereas the four lateral faces are considered impermeable), which obeys Darcy's law. By rotating the sample, permeability has been calculated in the three space directions (Table 3).

3. Results

3.1. Syn-decompression degassing

Here we address samples with crystallinity (ψ) < 20 vol%, which degassed in response to quasi-continuous decompression without dwell time at P_f (Table 2).

3.1.1. Final pressure of 10–15 MPa

The bubbles in the 850SYN10 series (*Supplementary Information_B*a) show comparable sizes, very tortuous outlines, and strong features of coalescence with bending and dimpling melt–bubble walls as described by Castro et al. (2012a) (Fig. 2a). Note here that we interpret these melt–bubble wall characteristics as coalescence rather than quench-induced bubble resorption as described by McIntosh et al. (2014), since the very fast quench times of 1–2 s of our experiments prevent texture evolution during cooling. Φ starts decreasing from $80_{\pm5}$ vol% for a decompression duration of ~1 h to $50–60_{\pm5}$ vol% for 30 h or more (blue circles, Fig. 3a). The measured Φ of $80_{\pm5}$ vol% is in agreement within error with the gas fraction (α) of 84 vol% calculated for a closed-system equilibrium degassing (Table 4). During this phase of general Φ-decrease, D_{max} remains constant and high (~500 µm) before dropping to ~200–300 µm after ~200 h (blue circles, Fig. 3b). Meanwhile, $\log N_v$ slightly decreases from ~13 to 12 m^{-3} before drastically dropping after ~200 h of decompression (down to $10^{10.5}$ m^{-3} for ~1000 h; blue circles, Fig. 3c).

The permeability calculated in the sample decompressed in 72 h is $\sim10^{-10.2}$ m^2 (D33; Table 3).

3.1.2. Final pressure of 30 MPa

The bubbles in the 850SYN30 series are sub-spherical for decompression durations up to 48 h, but elongate and display tortuous outlines when decompressed in 72 h (*Supplementary Information_B*b). Bubble size visibly increases with increasing decompression duration. The sample decompressed within 1.5 h reveals several bubble coalescence features with stretching and dimpling melt–bubble walls following Castro et al.'s (2012a) nomenclature (Fig. 2b). Φ of $47–49_{\pm5}$ vol% measured in the H_2O-undersaturated runs and Φ ~55 vol% measured in the H_2O-saturated runs are in agreement with their respective α within analytical error (α of 54–55 vol% for the H_2O-undersaturated runs and 58 vol% for the H_2O-saturated ones; Table 4) and thus compatible with an equilibrium degassing (green triangles, Fig. 3a). For decompression durations of 1–10 h, D_{max} is 100–200 µm (green triangles, Fig. 3b) and $\log N_v$ is ~13.5 m^{-3} (green triangles, Fig. 3c). For decompression duration >10 h, Φ stays at a plateau value of 55 vol% (i.e. equilibrium degassing), while D_{max} increases up to 320 µm (plateau value at ~20 h; green triangles, Fig. 3b) and N_v decreases drastically (green triangles, Fig. 3c).

The permeability calculated in the sample decompressed in 3 h is $\sim10^{-13.2}$ m^2 (D3; Table 3).

3.1.3. Final pressure of 50 MPa

The bubbles in the 850SYN50 series are sub-spherical and increase in size with increasing decompression duration. The series show overall very few features of bubble coalescence (*Supplementary Information_B*c). Φ reaches 25–30 vol% within less than 1-h decompression time and stays at this plateau value at least during decompression durations of 100–200 h (red diamonds, Fig. 3a). The Φ plateau value of $25–30_{\pm4}$ vol% is close to $\alpha = 35$ vol% expected for an equilibrium degassing (Table 4). During the period of Φ increase (decompression duration <1 h), D_{max} is ~80 µm (red diamonds, Fig. 3b) and a maximum $\log N_v$ of 13.7–14.3 m^{-3} is reached (red diamonds, Fig. 3c). As soon as Φ reaches 25–30 vol%,

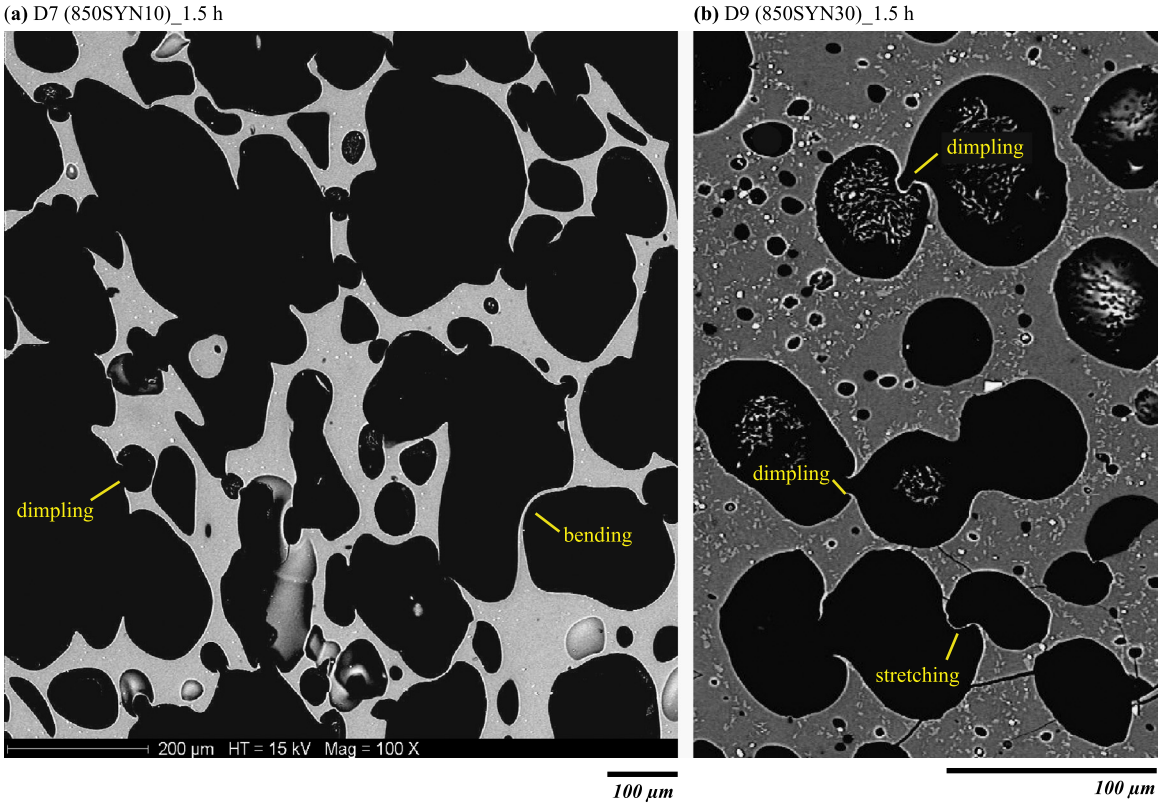

Fig. 2. Features of bubble coalescence in samples decompressed at 850 °C over 1.5 h showing bubble–melt wall thinning by bending, stretching, and dimpling, following Castro et al.'s (2012a, 2012b) nomenclature (a) D7 from 850SYN10 and (b) D9 from 850SYN30.

Table 4
Gas fraction and viscosity calculations.

Starting glass[a]	Run	T (°C)	Before decompression				After decompression					
			P_i (MPa)	C_{wi}[b] (wt%)	P_{sat}[c] (MPa)	$\log \eta_i$[d] (Pa s)	P_f (MPa)	C_{wf}[b] (wt%)	α[c,e]	$\log \eta_{melt}$[d] (Pa s)	Ca[f]	$\log \eta_{bulk}$[g] (Pa s)
HTN	HTN1–HTN5	875	200	5.7	200	4.3	50	2.6	0.42	5.9	1.5	4.2
SHILL	SH1–SH16	860	150	4.9*	150	4.6	50	2.6	0.34	5.7	1.0	5.5
RHY	A1–A9	875	200	5.7	200	4.2	50	2.6	0.42	5.7	1.5	4.1
RHY	D2–D3	850	200	5.2	165	4.6	30	2.0	0.54	6.4	1.0	6.2
RHY	D9	850	200	5.4	175	4.6	30	2.0	0.55	6.4	1.0	6.2
RHY	D4, D6, D38	850	200	5.6	185	4.5	10	1.1	0.84	7.3	2.5	4.9
RHY	D20	850	200	5.8*	200	4.4	60	2.9	0.34	5.8	1.0	5.9
RHY	D25–D27, D34, D39	850	200	5.8*	200	4.4	30	2.0	0.58	6.4	1.0	6.2
RHY	D7, D12, D33, D35	850	200	5.8*	200	4.4	10	1.1	0.85	7.3	2.5	5.1
RHY	VP2–VP10, VP14	850	200	5.1	160	4.7	50	2.6	0.35	6.0	1.0	5.8
RHY	VP13, VP18	850	200	5.1	160	4.7	15	1.3	0.74	7.0	2.0	4.6
Pel-Pumice		875	240	6.5	240	4.1	25	1.8	0.69	6.3	2.5	5.2
Pel-Surge		875	240	6.5	240	4.1	15	1.3	0.80	6.7	1.5	3.8
Pin-White		780	220	6.0	220	5.0	11	1.2	0.82	8.0	2.5	4.9
Pin-Grey		790	220	6.0	220	4.9	11	1.2	0.82	7.9	2.5	4.8

[a] HTN, SHILL, and RHY as in Table 1; Pel-Pumice and Pel-Surge are the residual melts of Mt Pelée P1 Plinian pumice and dome-related surges, respectively; Pin-White and Pin-Grey are the residual melts of Mt Pinatubo 1991 white and grey pumices, respectively.

[b] C_{wi} is initial melt H_2O content calculated at P_i and T either after Liu et al. (2005) for the H_2O-saturated or following the procedure of Martel (2012) for the H_2O-undersaturated samples; (*) denotes the presence of pre-decompression bubbles; C_{wf} is the melt H_2O content calculated at P_f and T after Liu et al. (2005).

[c] Saturation pressure calculated after Liu et al. (2005) for C_{wi}.

[d] Melt viscosity calculated at T after Giordano et al. (2008) to account for the differences in starting melt compositions (anhydrous), decreased by the viscosity difference between the anhydrous and hydrous haplogranite calculated after Hess and Dingwell (1996) (η_i for C_{wi} and η_{melt} for C_{wf}).

[e] Gas fraction calculated for a closed-system equilibrium degassing after Jaupart and Tait (1990) as $\alpha = (1 + \rho_w/((C_{wi} - C_{wf}) * \rho_m))^{-1}$, with ρ_m the melt density (taken as 2.2 g/cm^3; Knoche et al., 1995) and ρ_w water density calculated after Saul and Wagner (1989).

[f] Capillary number set to 1.0 at 850 °C and 30–50 MPa ($\eta_{bulk} \sim \eta_{melt}$), 1.5 at 875 °C, and 2.5 for $P_f = 10$ MPa (see text).

[g] Bulk viscosity calculated after Eq. (1) (see text).

D_{max} starts increasing up to 200 µm (red diamonds, Fig. 3b) and N_v decreases drastically (red diamonds, Fig. 3c).

The bubbles in the 860SYN50 series (*Supplementary Information_B*h) are sub-spherical for decompression duration up to 10 h, but display tortuous outlines for decompression durations longer than 100 h. Bubble size visibly increases with increasing decompression duration. The series shows overall very few features of coalescence for decompression durations shorter than 10 h. Φ in-

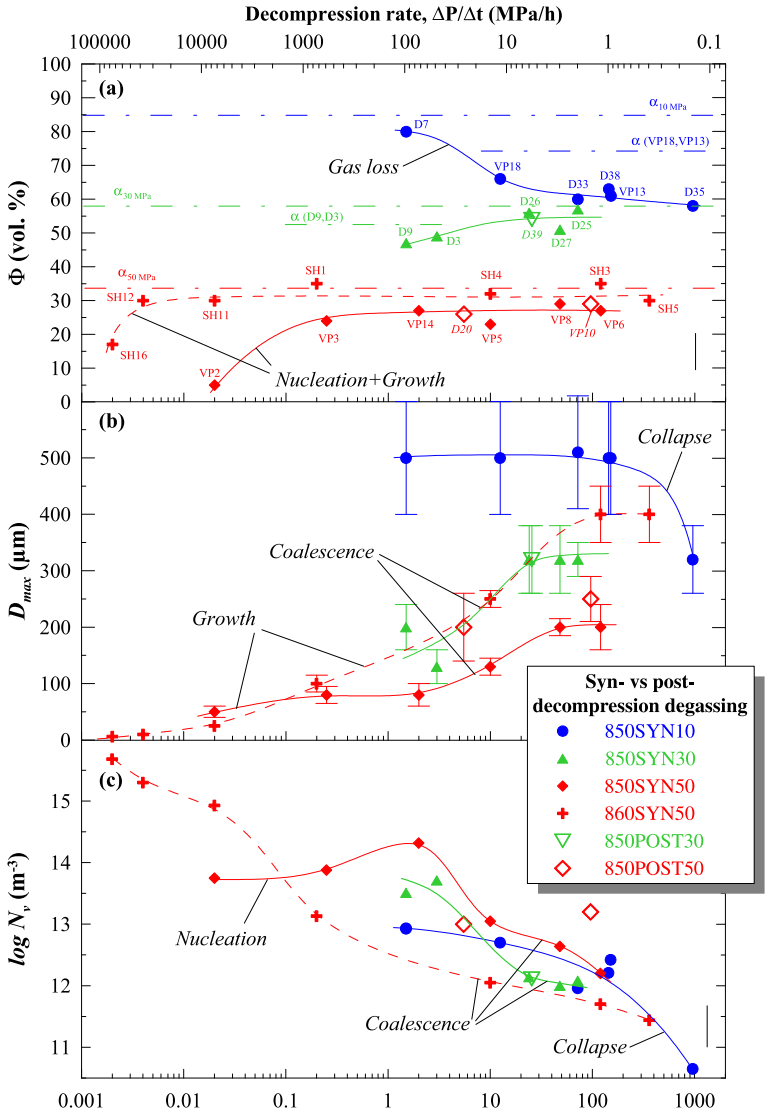

Fig. 3. Time evolution of the syn-decompression degassing (filled symbols; time is decompression duration) and post-decompression degassing (outlined symbols; time is time spent at P_f) showing (a) Φ, (b) D_{max}, and (c) N_v, for 850SYN50, 850SYN30, 850SYN10, and 860SYN50; The maximum error of the measurements is given by the black vertical lines on the right-hand side of the diagrams, except in (b). In (a), labels refer to the run numbers as in Table 1 and the dash–dot lines show α as given in Table 2; in (c), only the samples with crystal content $\psi \leq 16$ vol% are shown (see text for justification); 860SYN50 data from Martel and Schmidt (2003). (For interpretation of the references to color in this figure legend, the reader is referred to the web version of this article.)

creases up to 30–35$_{\pm 4}$ vol% after a decompression of only 12 s (red crosses, Fig. 3a). This Φ range is close to $\alpha = 34$ vol% calculated for an equilibrium degassing (Table 4). D_{max} constantly increases up to about 400 μm after about 120 h (red crosses, Fig. 3b), while N_v constantly decreases from $10^{15.7}$ to $10^{11.4}$ m^{-3} (red crosses, Fig. 3c).

3.2. Post-decompression degassing

We now address samples with crystallinities <20 vol% that mostly degassed during dwell times at P_f after a rapid decompression. Although mostly occurring during dwell time at P_f, the degassing likely started during decompression, so that the reference time starts at the beginning of the decompression (Table 2).

3.2.1. Samples decompressed at 850 °C

These samples belong to the 850POST30 and 850POST50 series. All samples show sub-rounded bubbles, even after more than 100 h spent at P_f, and many bubble coalescence features (*Supplementary Information_Be and Bf*). For all samples, Φ is close to the calculated α, i.e. 54$_{\pm 5}$ vol% against $\alpha = 58$ vol% for 850POST30 (green outlined triangle, Fig. 3a) and 26–29$_{\pm 4}$ vol% against $\alpha =$ 34–35 vol% for 850POST50 (red outlined diamonds, Fig. 3a). Log N_v is ~12.0 and ~13.1 m^{-3} in the samples decompressed to 30 MPa and 50 MPa, respectively (red outlined diamonds, Fig. 3c).

The permeability calculated in the sample that stayed 24 h at 30 MPa is ~$10^{-11.5}$ m^2 (D39; Table 3).

3.2.2. Samples decompressed at 875 °C ($P_f = 50$ MPa; $\Delta P/\Delta t = 1200$ MPa/h)

Bubbles in the 875POST50 series are sub-spherical and show coalescence features after a decompression duration of only 0.1 h (*Supplementary Information_Bg*). At this duration, Φ is 37$_{\pm 5}$ vol%, close to $\alpha = 42$ vol% expected at equilibrium (Table 4), D_{max} is ~125 μm, and log N_v is 13.4 m^{-3} (red filled circles, Fig. 4). However, after ~6 h spent at P_f, Φ drops below 10 vol%, D_{max} is <100 μm, and samples are nearly devoid of bubbles (log N_v ~ 11 m^{-3} after 2 days spent at P_f) (red filled circles, Fig. 4).

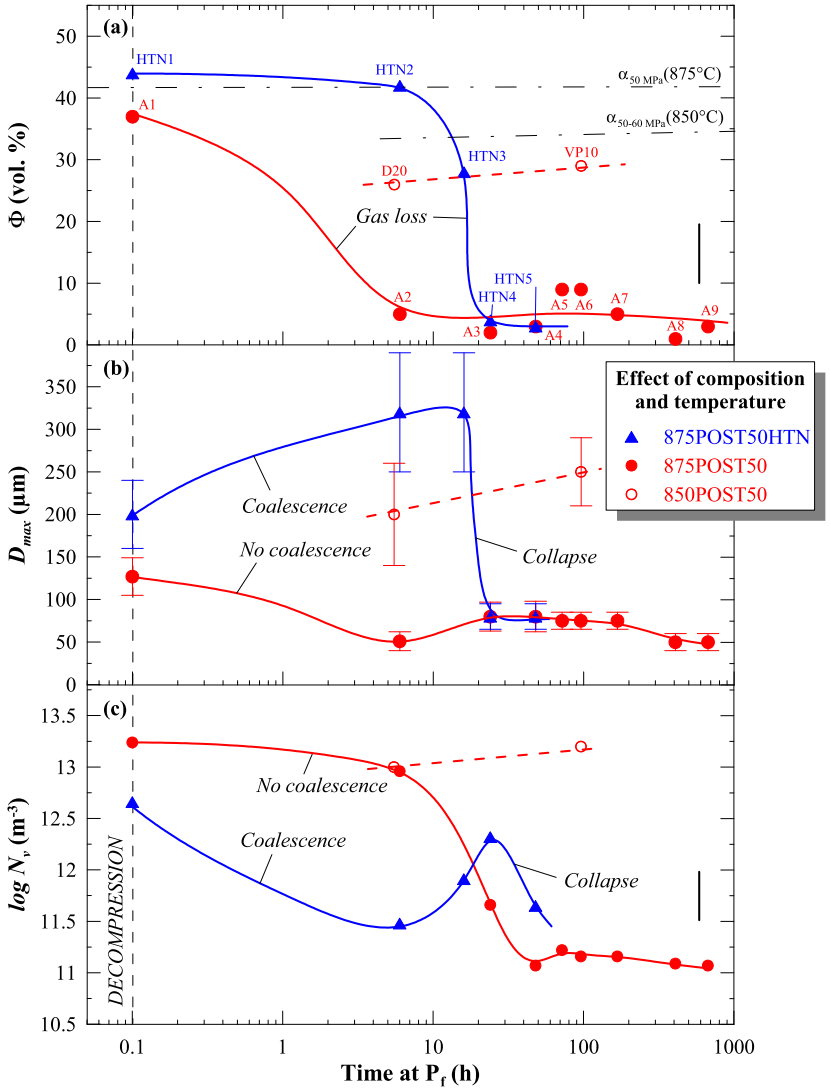

Fig. 4. Effect of melt composition on the time evolution of the post-decompression degassing showing (a) Φ, (b) D_{max}, and (c) N_v, for RHY and HTN rapidly decompressed ($\Delta P/\Delta t = 1200$ MPa/h) at 875 °C from 200 MPa to $P_f = 50$ MPa (filled symbols). RHY decompressed at 850 °C ($\Delta P/\Delta t = 93$–600 MPa/h; outlined symbols) is also shown to compare with RHY decompressed at 875 °C. The maximum error on the measurements is given by the black vertical lines on the right-hand side of the diagrams, except in (b). In (a), labels refer to the run numbers as in Table 1 and the dash–dot line shows α as given in Table 2. (For interpretation of the references to color in this figure legend, the reader is referred to the web version of this article.)

Bubbles in the 875POST50HTN series are sub-rounded, sometimes elongated, with increasing sizes for duration up to 16 h followed by a size decrease with increasing dwell time (Fig. 1). Φ is 42–44 vol% for 6 h spent at P_f, in agreement with $\alpha = 42$ vol% expected at equilibrium (Table 4), before dropping below 5 vol% for longer durations (blue triangles, Fig. 4a). For dwells shorter than 24 h, D_{max} increases from ~200 to 325 μm, before decreasing drastically to less than 100 μm for longer durations (blue triangles, Fig. 4b). Log N_v decreases from 12.7 m^{-3} after 0.1 h to ~11.5 m^{-3} after 6 h at P_f, before showing a peak at 12.3 m^{-3} for 1 day spent at $P_f = 50$ MPa (blue triangles, Fig. 4c).

3.3. Crystallized samples

Samples that crystallized more than 20 vol% of plagioclase microlites in response to long dwell times (>2 days) were not plotted in Fig. 3 and Fig. 4 and will be discussed separately (*Supplementary Information_C*). The permeability calculated in one crystallized sample from the 850POST30 series is ~$10^{-12.1}$ m^2 (D4; Table 3).

4. Discussion

4.1. Deciphering degassing and outgassing from the time-evolution curves of porosity, bubble diameter, and bubble number density

The degassing process primarily starts with an event of bubble nucleation. At the time of degassing, the starting melts (i) are crystal free or contain few plagioclase microlites that did not represent preferential sites for bubble nucleation (Hurwitz and Navon, 1994) and (ii) do not contain significant initial bubbles (<1 vol%). Therefore, we assume a decompression-induced homogeneous bubble nucleation event. Bubble nucleation implies a drastic increase of N_v, an increase of Φ because gas is being exsolved from the melt, whereas D_{max} stays nearly constant or increases slightly (because bubbles are not yet significantly growing).

Once nucleated, bubbles grow by the combined effect of H_2O diffusion from the melt to the bubble and decompression-induced gas expansion. Bubble growth implies increasing Φ and D_{max} at constant N_v because bubbles stop nucleating and do not significantly coalesce.

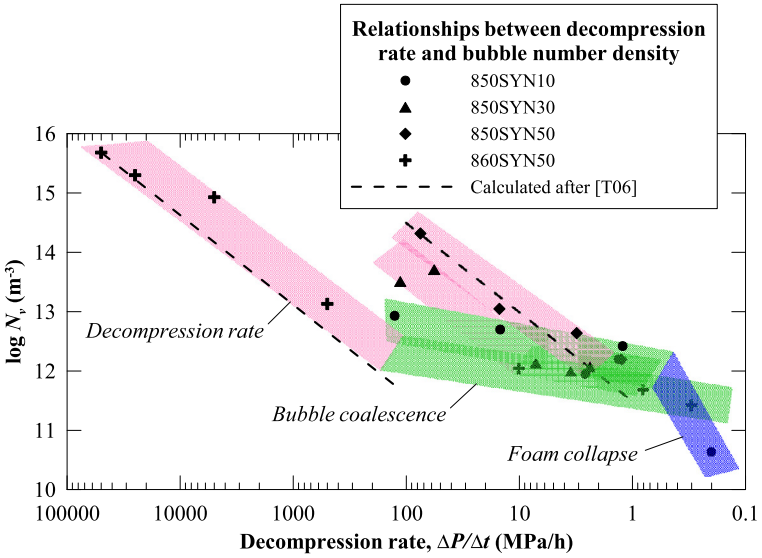

Fig. 5. Bubble number density dependence on decompression rate (extracted from Fig. 3c, starting from the highest N_v and showing only the samples with crystallinity <20 vol% that experienced syn-decompression degassing). The $N_v - \Delta P/\Delta t$ relationship has been divided into three linear trends (box widths correspond to the analytical error) marking the effects of (1) decompression rate (pink), (2) bubble coalescence (green), and (3) foam collapse (blue). The [T06] lines represent the trend calculated after Toramaru (2006) (see text). (For interpretation of the references to color in this figure legend, the reader is referred to the web version of this article.)

In-situ observations of degassing rhyolitic melts suggest that bubbles are not moving independently of the melt and stay roughly where they nucleated (Martel and Bureau, 2001), which is a combined consequence of the high viscosity of rhyolitic melts and short timescale of the experiments. During bubble growth, bubble–melt walls thin, eventually leading to bubble coalescence. The bending, stretching, and dimpling of bubble–melt walls (as in Fig. 2) are common features in experimental samples decompressed in less than ~1 h s to $P_f \leq 50$ MPa and rapidly quenched to prevent bubble relaxation and recovery to a spherical shape (Castro et al., 2012a). Bubble coalescence implies an increase of D_{max} and a general decrease of N_v, while Φ increases or remains constant depending on whether H_2O is still exsolving from the melt or not. By extensive coalescence, we mean a combined drastic decrease of N_v and increase of D_{max} with time, which for instance is the case for run D26 but not run D3 (green triangles, Fig. 3) even if coalescence features are observed in this sample (*Supplementary Information_B*).

Coalescing bubbles may eventually generate gas channels leading to a pervasive interconnectivity. At this point of high permeability to fluids, the magma either stays as a foam (e.g., pumices) or the gas escapes and the foam collapses (e.g. obsidian domes or rhyolitic lava flows; Westrich and Eichelberger, 1994). Outgassing and foam collapse imply a decrease in Φ commonly accompanied by drastic decreases in D_{max} and N_v.

4.2. Syn- versus post-decompression degassing

The few post-decompression degassing experiments show values of Φ, D_{max}, and N_v that are comparable within error to the syn-decompression degassing ones (outlined versus filled symbols, Fig. 3), which may be attributed to a similar degassing behavior over the time period investigated. This similarity could suggest that the degassing process mainly depends on time available, regardless of whether degassing occurs during or after decompression, and only to a lesser extent on decompression rate.

On the other hand, bubble number density at the moment of nucleation is predicted to correlate positively with decompression rate (Mourtada-Bonnefoi and Laporte, 1999, 2004). N_v measured in the series potentially recording bubble nucleation (i.e. 860SYN50 and 850SYN50; red crosses and red diamonds, respectively, in Fig. 3) at a decompression rate of 100 MPa/h suggest $\log N_v = 14.0_{\pm 0.5}$. This value is in good agreement with the estimation from in-situ decompression experiments using a rhyolitic melt free of bubble coalescence (Gondé et al., 2011). Applying the trend calculated by Toramaru (2006), we extrapolated N_v to lower decompression rates in order to calculate N_v at the time of nucleation for samples affected by later coalescence [using melt H_2O diffusion of 2.2×10^{-11} m/s calculated after Zhang and Behrens (2000) and gas/melt interfacial tension of 0.13 N/m calculated after Bagdassarov et al. (1999) at 850 °C and 5.9 wt% melt H_2O; note that using a gas/melt interfacial tension of 0.05 N/m that covers the range of hydrous magmas (Mangan and Sisson, 2005; Gondé et al., 2011) increases N_v by 1 log unit].

Our experimental data therefore show three different trends:

(i) A drastic decrease of N_v while D_{max} increases (pink trend in Fig. 5), which is in good agreement with the relationship calculated after Toramaru (2006) starting with $\log N_v = 15.5$ for a decompression rate of 50 000 MPa/h (860SYN50) and $\log N_v = 14.5$ for a decompression rate of 100 MPa/h (850SYN50). This trend is thus attributed to the effect of decompression rate on N_v where bubble coalescence is not significant;

(ii) A slight decrease of N_v while D_{max} is constant or increases where bubbles start to coalesce extensively (green trend in Fig. 5); at this point of extensive coalescence, the calculated $N_v - \Delta P/\Delta t$ relationships no longer hold. The observed trend thus reflects the evolution of N_v with bubble coalescence quasi-independently of $\Delta P/\Delta t$ (nearly horizontal trends).

(iii) A drastic decrease of both N_v and D_{max} (blue trend in Fig. 5) defined by 850SYN10 at a very slow decompression rate (0.2 MPa/h), most likely revealing bubble loss due to foam collapse.

4.3. Viscosity control on the time evolution of bubble growth, coalescence, and outgassing

The time evolution of the degassing process is controlled by melt composition, water content, temperature, bubble and crystal contents, which are all key parameters of viscosity.

4.3.1. Melt composition

Fig. 4 reveals a strong difference in the degassing behavior of HTN and RHY compositions. Both series started degassing in similar conditions (comparable D_{max} and N_v), but the collapse of the bubbly foam (indicated by a drastic drop in Φ and D_{max}) occurs within the first 6 h for RHY and after 12 h for HTN. Moreover, RHY does not show evidence of bubble growth or coalescence (decreasing D_{max} without N_v increase) before outgassing, while HTN does (constant Φ and increase of D_{max} while N_v decreases).

The difference in viscosity between the two starting materials calculated using the model of Giordano et al. (2008) is only ~0.2 log unit, mainly due to their difference of 3 wt% SiO_2 (Table 4), as the effect of ferromagnesian components on both melt viscosity and bubble–melt surface tension is not known. We speculate that the difference in silica and ferromagnesian content may explain the different outgassing timescales, with the more polymerized, more viscous, and ferromagnesian-free HTN degassing in equilibrium longer (more time for bubble growing and coalescence) than the silica-poorer, less viscous, and ferromagnesian-bearing RHY.

4.3.2. Temperature

Our results only partially reveal the effect of temperature on the degassing behavior, suggesting that increasing temperature by 25 °C favors early outgassing and subsequent foam collapse. Fig. 4 shows that experiments at 850 °C maintain equilibrium porosities, constant D_{max}, and constant N_v for more than 4 days, differently to those at 875 °C, which experience severe outgassing and loss of nearly all the bubbles after 48 h (drastic drop of Φ and decrease of N_v of more than 2 log units).

4.3.3. Final pressure

Final pressure controls two crucial parameters that affect melt viscosity: melt H_2O content and bubble content. The H_2O content of the melt only varies from 1.1 to 2.9 wt% for the investigated range of P_f (Table 4) and H_2O most strongly influences viscosity for contents <1.0 wt% (Hess and Dingwell, 1996). In contrast, vesicularity varies over a wide range from 0 to 80 vol% (Table 2). Samples decompressed to $P_f = 30$ and 50 MPa show equilibrium degassing followed by bubble coalescence without foam collapse for durations up to 300 h (Fig. 3). On the contrary, samples decompressed to 10 MPa start outgassing after 1.5 h and show extensive bubble coalescence followed by bubble collapse. This suggests that the rhyolitic foam generated by decompression to pressures <10 MPa (with $\Phi >$ ~60 vol% and D_{max} as large as ~500 μm) cannot survive longer than a couple of hours in our experimental conditions. Our experiments therefore seem to define a limiting Φ that controls foam lifetime by promoting early bubble coalescence, formation of channels of gas that eventually escape from the melt, producing foam collapse at low pressures.

4.3.4. Viscosity of the bubbly melt

The variations in temperature, melt composition, H_2O content, and bubble content can be gathered by the rheology of a multiphase suspension, making thus likely a relationship between the outgassing timescale and bulk viscosity (melt + bubbles) of the sample. The viscosity of the bubbly melt (η_{bulk}) is different from that of the pure melt (η_{melt}) because bubbles may act as solid or deformable particles that increase or decrease viscosity, respectively, depending on bubble size and shear conditions (Llewellin et al., 2002a; Rust and Manga, 2002). In our experimental conditions, the samples are unlikely to undergo very large strain. At low Φ, η_{melt} may be relevant to account for the outgassing timescale. In highly porous samples, however, elongated bubbles (Figs. 1 and 2a) suggest deformation (e.g. bubbles repulsing each other to accommodate their volume increase), and the outgassing timescale clearly shows inconsistencies where reported as a function of η_{melt}. For instance, samples decompressed to 10 MPa have the highest η_{melt} due to their low residual H_2O content (Table 4) but outgas well before other samples decompressed to 30 or 50 MPa. Moreover, the large difference in outgassing timescales (~90 h in samples decompressed to 50 MPa) cannot simply be accounted for by the 0.1–0.3 log unit difference in η_{melt} between 850 and 875 °C (Table 4). Therefore, other parameters than η_{melt} that are affected by temperature (surface tension at bubble–melt interface?) may be considered to render the observed degassing timescale. Besides η_{melt}, the key parameters controlling the viscosity of a bubbly suspension are bubble volume content and the capillary number, *Ca*, which describes the ratio of the viscous stress to the restoring stress: $Ca = (\eta_{melt}\dot{\gamma})/(\sigma/a)$, where $\dot{\gamma}$ is shear strain-rate, σ is the surface tension at the bubble–liquid interface, and a is the non-deformed bubble radius.

Following the review and analysis of the rheology of bubble-bearing magmas of Mader et al. (2013), we used Llewellin et al.'s (2002b) equation for steady, simple-shearing flow giving η_{bulk} as follows:

$$\eta_{bulk} = \eta_{melt} \times \eta_{r,\infty} + \frac{\eta_{r,0} - \eta_{r,\infty}}{1 + (K\,Ca)^m} \quad (1)$$

where $\eta_{r,0} = (1-\alpha)^{-1}$ is the limiting relative viscosity of the concentrated suspensions at low *Ca*, $\eta_{r,\infty} = (1-\alpha)^{5/3}$ is the limiting relative viscosity of the concentrated suspension at high *Ca*, $K = 6/5$, and $m = 2$ for a monodisperse bubble distribution. We cannot precisely determine *Ca* for our experiments, because (i) strain rate is not measured, (ii) we would need the radius of the non-deformed bubble prior to coalescence, but bubbles already extensively coalesced in the samples decompressed to 10 MPa. Even approximating *Ca* by the Taylor deformation parameter (valid for small *Ca* where bubbles are ellipsoidal and calculated using the length of the semi-axes of the ellipsoid that best fits the bubble shape) would be useless, since bubbles may have had time to relax and recover a pseudo-spherical shape before quenching. We therefore set *Ca* to ~1.1 for the experiments at 850–860 °C, 30 and 50 MPa, in order to keep η_{bulk} close to η_{melt} (i.e. no significant effect of the bubbles). *Ca* was set to 1.5 for the two series at 875 °C and to 2.5 for the samples decompressed to 10 MPa, in order to obtain $\eta_{bulk} < \eta_{melt}$. We assume that both high temperature and large bubble size increases *Ca* by facilitating bubble deformation and decreasing liquid–vapor surface tension. The calculated η_{bulk} using (1) are reported in Table 4.

Reported in η_{bulk}-time space, the data allow identification of different stages of the decompression-induced degassing process (Fig. 6). The stage where the bubbles are in a process of nucleation and growth ($\Phi < \alpha$; no coalescence) is restricted to times <0.03 h for $\eta_{bulk} \sim 10^{5-6}$ Pa s. For longer duration, degassing reaches equilibrium ($\Phi \sim \alpha$), with a threshold of extensive coalescence occurring between 0.1 h for $\eta_{bulk} \sim 10^4$ Pa s and ~10 h for $\eta_{bulk} \sim 10^7$ Pa s. Outgassing starts where Φ becomes lower than α (reflecting gas loss). The outgassing field is restricted to low η_{bulk} and long durations, i.e. from 5 to 10 h for $\eta_{bulk} < 10^4$ Pa s to >1000 h for $\eta_{bulk} \sim 10^{5.5}$ Pa s. Foam collapse delimits an area from ~10 h for $\eta_{bulk} \sim 10^4$ Pa s to ~1000 h for $\eta_{bulk} \sim 10^5$ Pa s.

Another parameter (beyond the scope of this paper) that may shift bulk viscosity is the presence of crystals, which is discussed in *Supplementary Information_C*.

4.4. Time relationships between permeability, bubble coalescence, and foam collapse

The percolation theory for randomly placed monodisperse bubbles predicts a strong increase in permeability at ~30 vol% (e.g. Sahimi, 1994). Yet, the permeability–porosity relationships in natural and experimental samples differ from the idealized percolation theory, with permeability increasing less abruptly at porosities

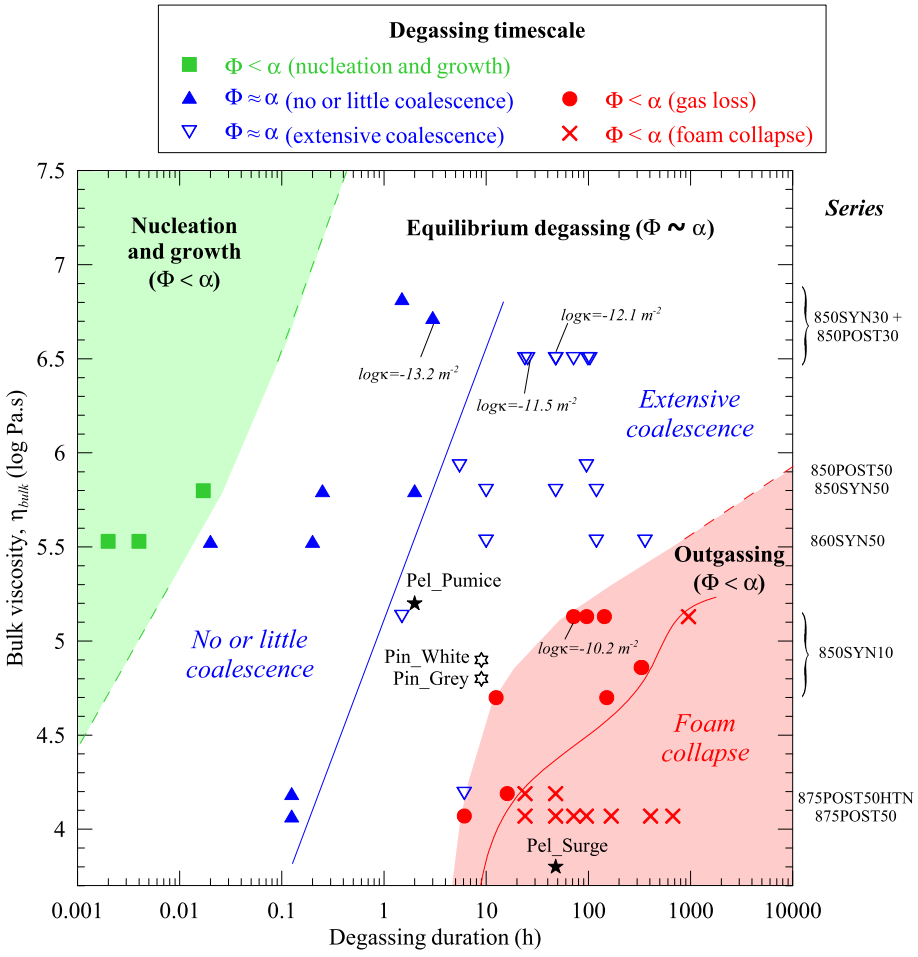

Fig. 6. Effect of the viscosity of the bubbly melt on the degassing timescale. η_{bulk} has been calculated using Eq. (1) (with η_{melt}, α, and Ca given in Table 4). The degassing process has been divided into three main stages: bubble nucleation and growth for which $\Phi < \alpha$ at short degassing durations, equilibrium degassing for which Φ approximates α (including a phase of major coalescence), and outgassing for which $\Phi < \alpha$ (including a phase of foam collapse) at long degassing durations. The filled stars represent the pumice and surge samples (Pel_Pumice and Pel_Surge) from the P1 (650 B.P.) eruption of Mt Pelée and the outlined stars represent the white and the grey pumice (Pin_White and Pin_Grey) of the 1991 Plinian pumice falls of Mt Pinatubo (see text).

from 30 up to 80 vol% (Blower, 2001). The permeability–porosity relationships often follow power law relationships with an exponent depending on the pore geometry (e.g. Wright et al., 2009).

Other factors have been demonstrated to contribute to the variation of the percolation threshold in magmas, such as melt viscosity, aperture size between pores (e.g. Bouvet de Maisonneuve et al., 2009), shear stresses (e.g. Okumura et al., 2009), distinct structures between expanding and collapsing bubbles (Rust and Cashman, 2004), and bubble size distribution. We could not systematically investigate the permeability evolution with porosity in our samples but we were able to measure permeability of 3 log unit differences for samples with comparable porosities of 50–60 vol% (Table 3). This suggests that in our experiments, time is an additional controlling factor that allows the vesicular melt to coalesce, become permeable and outgas.

A κ threshold of $\sim 10^{-13}$ m^2 at Φ ~50 vol% for vesicular foam just before extensive coalescence is provided by run D3 from 850SYN30 (Fig. 6): this sample has a Φ of $49_{\pm 5}$ vol% and the bubbles are sub-spherical and uniformly sized. Such a low connectivity, in the range of natural vesicular pyroclasts (commonly between 10^{-14} and 10^{-11} m^2; Mueller et al., 2005), associated to a relatively high porosity, may partly result from the uniform bubble size distribution in the sample (as previously suggested for breadcrust bombs; Mueller et al., 2005), but also from the short experimental duration (3 h at final pressure).

Runs D39 and D34 from 850POST30 have Φ of $51_{\pm 5}$ and $54_{\pm 5}$ vol%, respectively, and show strong coalescence features within 2 days. $\kappa \sim 10^{-12}$ m^2 calculated for both samples gives a typical value for foamed ($\Phi = 50$–60 vol%), permeable, but not yet outgassed, samples (Fig. 6). Similarly at lower η_{bulk}, D7 from 850SYN/POST10 is a highly porous ($\Phi = 80$ vol%) and likely highly permeable sample (Fig. 2a) that did not collapse within 1.5-h (Fig. 6). $\kappa \sim 10^{-10}$ m^2 calculated in D33 from 850SYN10 gives a threshold value for an outgassed sample that did not fully collapse in 3 days. These results highlight that κ alone is not a sufficient criterion to decipher gas loss and foam collapse, and that η_{bulk} and time are crucial parameters to take into account to understand whether highly permeable silicic foams can collapse after tens or hundreds of hours spent at final pressure.

4.5. Implications for explosive versus effusive eruption dynamics

Regardless of the large uncertainty inherent to the bulk viscosity calculation of bubble-bearing melts, our experiments suggest that time–viscosity relationships control degassing and outgassing (Fig. 6). Considering time as a key parameter for outgassing could explain, at least in some cases, why magmas with similar bulk rock compositions and initial volatile contents may erupt explosively as pumice (short-lived foam) or effusively as dense material (long-lived foam that eventually collapses) during the same eruptive sequence on a given volcanic system.

4.5.1. Experiment-nature scaling

The application of the experimental results to natural cases requires much thought regarding scaling of the process of bubble connectivity development. From a strictly physical point of view and ignoring any border effects, outgassing and foam collapse occur when the gas connectedness is pervasive. It is reasonable to believe that outgassing and foam collapse timescales compare in small (sample capsules) and large volumes (e.g. natural volcanic conduits), since bubble coalescence proceeds simultaneously at the sample interior and edge. A second concern is the role of the experimental container on the ability of gas to escape the melt. The difficult question to answer is whether the processes of bubble connection, outgassing and foam collapse are slowed down by the impermeable capsule. Our simulations are probably not unrealistic because impermeable country-rocks at conduit walls also exist in nature, i.e. sealed by silica-phase deposits (Sparks, 1997) or melted through viscous heating during high stresses (Hess et al., 2008).

The major difference between experimental and natural conditions in a volcanic conduit is the amount of deformation experienced by the bubbly melt. In a volcanic conduit, large deformation is expected at conduit walls. This would make the capillary number a crucial parameter in the bulk viscosity calculation and the degassing process. Indeed, the gas permeability of a non-deformed magma is a few to several orders of magnitude lower than for deformed and flowing magmas, in which outgassing is therefore drastically enhanced (Okumura et al., 2012; Toramaru, 2014). Yet, in-situ deformation experiments showed that shear localizes along the sample edges leaving the sample interior poorly-sheared and poorly-outgassed (Okumura et al., 2013). Thus, our experiments may be relevant for simulating decompression of the interior of a magma column.

In nature, however, foam collapse is not the only process to generate effusive silicic volcanism. Recent works on explosive–effusive transitions have explored the role of shear fracturing in causing non-explosive magma degassing (e.g. Gonnermann and Manga, 2003; Castro et al., 2012b, 2014).

4.5.2. Application to the case of Mt Pelée, Martinique

The P1 eruption (650 B.P.) of Mt Pelée produced a surge deposit of dense clasts followed by climactic Plinian pumice fallout. P1 pre-eruption conditions were estimated to be ~875 °C, ~200 MPa, and $6.5_{\pm 0.5}$ wt% H_2O dissolved in the melt (Martel et al., 1998). The pumice residual melt is rhyolitic and shows typical H_2O contents of $1.8_{\pm 0.3}$ wt%, suggesting a calculated α for an assumed close-system equilibrium degassing of $69_{\pm 5}$ vol%, in good agreement with the measured Φ of $71_{\pm 4}$ vol% (Martel et al., 2000). The P1 Plinian residual melt has an η_{bulk} of $10^{5.2}$ Pa s calculated after (1) for a Ca of 1.5 (875 °C – $P_f = 25$ MPa; Table 4) and Plinian events commonly last only few hours (Rutherford and Gardner, 2000; Castro and Dingwell, 2009), which make the P1 pumice plot in the "Equilibrium degassing – Extensive coalescence" field of Fig. 6 (very close to D7 sample that is texturally very similar; Fig. 2a). This is in a good agreement with the fact that pumice samples show strong coalescence features but no significant bubble loss ($\Phi \sim \alpha$).

In contrast, the dense clasts from the surges (1902 May 8th or P1) and block-and-ash flows (1902 and 1929), for which the eruption durations have been estimated experimentally to more than 2 days (Martel, 2012), show Φ of ~35 vol% (Martel et al., 2000). This suggests outgassing given that the pre-eruption conditions are similar to those of the P1 Plinian event (Martel et al., 1998). Although H_2O contents of the residual melts are difficult to estimate because the matrixes extensively crystallized, contents up to 1.3 wt% H_2O have been measured in the glassy matrix of P1 surge lithics (Martel et al., 2000); this would give an α of 80 vol%. The vesiculated P1 surge residual melt has an η_{bulk} of $10^{3.8}$ Pa s calculated after (1) for a Ca of 2.5 (875 °C – $P_f = 15$ MPa; Table 4), and therefore plots in the "Outgassing–Foam collapse" field of Fig. 6. This corroborates the hypothesis of a combined control of bulk viscosity and degassing timescale on the transition from pumices to bubble-deficient pyroclasts at Mt Pelée.

Permeability measurements are significantly different for the P1 Plinian pumices and 1929 dome samples: 10^{-12} and $10^{-9.5 \text{ to } -12}$ m^2, respectively (Jouniaux et al., 2000). These permeabilities are in agreement with our values obtained for (i) samples degassed at equilibrium and showing bubble coalescence ($10^{-11.5 \text{ to } -12.1}$ m^2) and (ii) outgassed and collapsed samples ($<10^{-10.2}$ m^2).

Nevertheless, we show in the *Supplementary Information_C* how microlite crystallization may play a role in degassing, outgassing, and foam collapse. The 1902 surge magmas of Mt Pelée crystallized microlites at very shallow level (Martel and Poussineau, 2007), therefore, the influence of a framework of both phenocrysts and microlites (~45 and ~30 vol%, respectively, for Mt Pelée surge pyroclasts) should be taken into account in the calculation of the bulk viscosity to better assess the global degassing process.

4.5.3. Application to the case of Mt Pinatubo, Philippines

The climactic event of Mt Pinatubo, 15 June 1991, lasted for 9 h (Wolfe and Hoblitt, 1996) and produced two varieties of Plinian pumice: a white phenocryst-rich and a grey phenocryst-poor pumice (Hoblitt et al., 1996). The pre-eruptive conditions were estimated to be ~780 °C, $200_{\pm 20}$ MPa, and a melt H_2O content ~6.0 wt% (Scaillet and Evans, 1999). H_2O measurements in the rhyolitic residual glass of the white pumice give an average of 1.2 wt% (Borisova et al., 2006), indicating efficient degassing, corroborated by high vesicularities of ~80 vol% and ~70 vol% measured in white and grey pumice clasts, respectively (Polacci et al., 2001). The textural differences of the matrix of white and grey pumice (content and number density of bubbles and microlites) was interpreted as resulting from different flow conditions in the volcanic conduit (Polacci et al., 2001): strong viscous dissipation at the conduit walls was proposed to generate the grey pumice by reheating (Polacci et al., 2001). The intensity of the reheating is not clearly quantified, but rheological experiments in a viscometer suggest temperature increase <10 °C for applied strain rates on the order of 10^{-3} s^{-1} (Hess et al., 2008).

The vesicular melt from the white and grey pumice has a η_{bulk} of $10^{4.9}$ and $10^{4.8}$ Pa s, respectively, calculated after (1) for a Ca of 2.5 ($P_f = 11$ MPa) with (i) their respective residual melt compositions (Polacci et al., 2001), (ii) 780 and 790 °C, respectively, and (iii) α of 0.82 calculated for a residual melt H_2O content of 1.2 wt% (Table 4). Both the white and grey samples plot in the "Equilibrium degassing–Extensive coalescence" field of Fig. 6 (close to the outgassing field), in agreement with pumiceous samples. This suggests that 1991 Mt Pinatubo magmas did not significantly outgas due to their rather high viscosity (and low temperature), despite their high vesicularities.

Acknowledgements

We are grateful to E. Mollard and A. Radadi Ali for their contribution to the decompression experiments, A. Kushnir for discussion on porosity and permeability, I. Di Carlo for help with the SEM, and A. Burgisser for assistance with the X-ray tomograph and the permeability calculations. We sincerely thank I. McIntosh and an anonymous reviewer for their careful reviews that undeniably improved the manuscript. This work benefited by the financial support of the Agence Nationale de la Recherche (contract No. ANR-05-CATT-0004 to C. Martel).

Appendix A. Supplementary material

Supplementary material related to this article can be found online at http://dx.doi.org/10.1016/j.epsl.2014.12.010.

References

Bagdassarov, N.S., Dorfman, A., Dingwell, D.B., 1999. Effect of alkalis, phosphorus and water on the surface tension of haplogranite melt. Am. Mineral. 85, 33–40.

Barclay, J., Riley, D.S., Sparks, R.S.J., 1995. Analytical models for bubble growth during decompression of high viscosity magmas. Bull. Volcanol. 57, 422–431.

Blower, J.D., 2001. Factors controlling permeability-porosity relationships in magma. Bull. Volcanol. 63, 497–504.

Blower, J.D., Keating, J.P., Mader, H.M., Phillips, J.C., 2002. The evolution of bubble size distributions in volcanic eruptions. J. Volcanol. Geotherm. Res. 120, 1–23.

Borisova, A.Y., Pichavant, M., Polvé, M., Wiedenbeck, M., Freydier, R., Candaudap, F., 2006. Trace element geochemistry of the 1991 Mt. Pinatubo silicic melts, Philippines: implications for ore-forming potential of adakitic magmatism. Geochim. Cosmochim. Acta 70, 3702–3716.

Bouvet de Maisonneuve, C., Bachmann, O., Burgisser, A., 2009. Characterization of juvenile pyroclasts from the Kos Plateau Tuff (Aegean Arc): insights into the eruptive dynamics of a large rhyolitic eruption. Bull. Volcanol. 71, 643–658.

Burgisser, A., Gardner, J.E., 2005. Experimental constraints on degassing and permeability in volcanic conduit flow. Bull. Volcanol. 67, 42–56.

Castro, J.M., Bindeman, I.N., Tuffen, H., Schipper, C.I., 2014. Explosive origin of silicic lava: textural and δD–H_2O evidence for pyroclastic degassing during rhyolite effusion. Earth Planet. Sci. Lett. 405, 52–61.

Castro, J.M., Burgisser, A., Schipper, C.I., Mancini, S., 2012a. Mechanisms of bubble coalescence in silicic magmas. Bull. Volcanol. 74, 2339–2352.

Castro, J.M., Cordonnier, B., Tuffen, H., Tobin, M.J., Puskar, L., Martin, M.C., Bechtel, H.A., 2012b. The role of melt-fracture degassing in defusing explosive rhyolite eruptions at volcan Chaiten. Earth Planet. Sci. Lett. 333–334, 63–69.

Castro, J.M., Dingwell, D.B., 2009. Rapid ascent of rhyolitic magma at Chaiten volcano, Chile. Nature 461, 780–783.

Degruyter, W., Bachmann, O., Burgisser, A., 2010. Controls on magma permeability in the volcanic conduit during the climactic phase of the Kos Plateau Tuff eruption (Aegean Arc). Bull. Volcanol. 72, 63–74.

Eichelberger, J.C., Carrigan, C.R., Westrich, H.R., Price, R.H., 1986. Non-explosive silicic volcanism. Nature 323, 598–602.

Gardner, J.E., 2007. Bubble coalescence in rhyolitic melts during decompression from high pressure. J. Volcanol. Geotherm. Res. 166, 161–176.

Gardner, J.E., Hilton, M., Carroll, M.R., 1999. Experimental constraints on degassing of magma: isothermal bubble growth during continuous decompression from high pressure. Earth Planet. Sci. Lett. 168, 201–218.

Giordano, D., Russell, J.K., Dingwell, D.B., 2008. Viscosity of magmatic liquids: a model. Earth Planet. Sci. Lett. 271, 123–134.

Gondé, C., Martel, C., Pichavant, M., Bureau, H., 2011. In situ bubble vesiculation in silicic magmas. Am. Mineral. 96, 111–124.

Gonnermann, H.M., Manga, M., 2003. Explosive volcanism may not be an inevitable consequence of magma fragmentation. Nature 426, 432–435.

Hamada, M., Laporte, D., Cluzel, N., Koga, K.T., Kawamoto, T., 2010. Simulating bubble number density of rhyolitic pumices from Plinian eruptions: constraints from fast decompression experiments. Bull. Volcanol. 72, 735–746.

Hess, K.-U., Cordonnier, B., Lavallee, Y., Dingwell, D.B., 2008. Viscous heating in rhyolite; an in situ experimental determination. Earth Planet. Sci. Lett. 275, 121–126.

Hess, K.-U., Dingwell, D.B., 1996. Viscosities of hydrous leucogranitic melts: non-Arrhenian model. Am. Mineral. 81, 1297–1300.

Higgins, M.D., 2000. Measurement of crystal size distributions. Am. Mineral. 85, 1105–1116.

Hoblitt, R.P., Wolfe, E.W., Scott, W.E., Couchman, M.R., Pallister, J.S., Javier, D., 1996. The preclimactic eruptions of Mt Pinatubo, June 1991. In: Newhall, C.G., Punongbayan, R.S. (Eds.), Fire and Mud: Eruptions and Lahars of Mount Pinatubo. University of Washington Press, Seattle, pp. 457–512.

Hurwitz, S., Navon, O., 1994. Bubble nucleation in rhyolitic melts: experiments at high pressure, temperature, and water content. Earth Planet. Sci. Lett. 122, 267–280.

Jaupart, C., Tait, S., 1990. Dynamics of eruptive phenomena. In: Nicholls, J., Russell, J.K. (Eds.), Modern Methods of Igneous Petrology: Understanding Magmatic Processes. In: Mineral. Soc. Am. Rev., vol. 24, pp. 213–238.

Jouniaux, L., Bernard, M.-L., Zamora, M., Pozzi, J.-P., 2000. Streaming potential in volcanic rocks from Mount Pelée. J. Geophys. Res. 105 (B4), 8391–8401.

Klug, C., Cashman, K.V., 1994. Vesiculation of May 18, 1980, Mount St. Helens magma. Geology 22, 468–472.

Klug, C., Cashman, K.V., 1996. Permeability development in vesiculating magmas: implications for fragmentation. Bull. Volcanol. 58, 87–100.

Knoche, R., Dingwell, D.B., Webb, S.L., 1995. Melt densities for leucogranites and granitic pegmatites: partial molar volumes for SiO_2, Al_2O_3, Na_2O, K_2O, Li_2O, Rb_2O, Cs_2O, MgO, CaO, SrO, BaO, B_2O_3, P_2O_5, F_2O_{-1}, TiO_2, Nb_2O_5, Ta_2O_5, and WO_3. Geochim. Cosmochim. Acta 59 (22), 4645–4652.

Larsen, J.F., Denis, M.-H., Gardner, J.E., 2004. Experimental study of bubble coalescence in rhyolitic and phonolitic melts. Geochim. Cosmochim. Acta 68, 333–344.

Larsen, J.F., Gardner, J.E., 2000. Experimental constraints on bubble interactions in rhyolite melts: implications for vesicle size distributions. Earth Planet. Sci. Lett. 180, 201–214.

Launeau, P., Cruden, A.R., 1998. Magmatic fabric acquisition mechanisms in a syenite: results of a combined anisotropy of magnetic susceptibility and image analysis study. J. Geophys. Res. 103, 5067–5089.

Launeau, P., Robin, P.-Y., 1996. Fabric analysis using the intercept method. Tectonophysics 267, 91–119.

Liu, Y., Zhang, Y., 2000. Bubble growth in rhyolitic melt. Earth Planet. Sci. Lett. 181, 251–264.

Liu, Y., Zhang, Y., Behrens, H., 2005. Solubility of H_2O in rhyolitic melts at low pressures and a new empirical model for mixed H_2O–CO_2 solubility in rhyolitic melts. J. Volcanol. Geotherm. Res. 143, 219–235.

Llewellin, E.W., Mader, H.M., Wilson, S.D.R., 2002a. The rheology of a bubbly liquid. Proc. R. Soc. A 458, 987–1016.

Llewellin, E.W., Mader, H.M., Wilson, S.D.R., 2002b. The constitutive equation and flow dynamics of bubbly magmas. Geophys. Res. Lett. 29, 2170.

Lyakhovsky, V., Hurwitz, S., Navon, O., 1996. Bubble growth in rhyolitic melts: experimental and numerical investigation. Bull. Volcanol. 58, 19–32.

Mader, H.M., Llewellin, E.W., Mueller, S.P., 2013. The rheology of two-phase magmas: a review and analysis. J. Volcanol. Geotherm. Res. 257, 135–158.

Mangan, M., Sisson, T., 2000. Delayed, disequilibrium degassing in rhyolite magma: decompression experiments and implications for explosive volcanism. Earth Planet. Sci. Lett. 183, 441–445.

Mangan, M., Sisson, T., 2005. Evolution of the melt–vapor surface tension in silicic volcanic systems: experiments with hydrous melts. J. Geophys. Res. 110, B01202. http://dx.doi.org/10.1029/2004JB003215.

Martel, C., 2012. Eruption dynamics inferred from microlite crystallization experiments: application to Plinian and dome-forming eruptions of Mt. Pelée (Martinique, Lesser Antilles). J. Petrol. 53, 699–725.

Martel, C., Bourdier, J.-L., Pichavant, M., Traineau, H., 2000. Textures, water content and degassing of silicic andesites from recent plinian and dome-forming eruptions at Mt Pelée volcano (Martinique, Lesser Antilles arc). J. Volcanol. Geotherm. Res. 96, 191–206.

Martel, C., Bureau, H., 2001. In-situ high-pressure and high-temperature bubble growth in silicic melts. Earth Planet. Sci. Lett. 191, 115–127.

Martel, C., Pichavant, M., Bourdier, J.-L., Traineau, H., Holtz, F., Scaillet, B., 1998. Magma storage conditions and control of eruption regime in silicic volcanoes: experimental evidence from Mt. Pelée. Earth Planet. Sci. Lett. 156, 89–99.

Martel, C., Poussineau, S., 2007. Diversity of eruptive style inferred from the microlites of Mt. Pelée andesite (Martinique, Lesser Antilles). J. Volcanol. Geotherm. Res. 166, 233–254.

Martel, C., Schmidt, B.C., 2003. Decompression experiments as an insight into ascent rates of silicic magmas. Contrib. Mineral. Petrol. 144, 397–415.

McIntosh, I.M., Llewellin, E.W., Humphreys, M.C.S., Nichols, A.R.L., Burgisser, A., Schipper, C.I., Larsen, J.F., 2014. Distribution of dissolved water in magmatic glass records growth and resorption of bubbles. Earth Planet. Sci. Lett. 401, 1–11.

Mollard, E., Martel, C., Bourdier, J.-L., 2012. Decompression-induced experimental crystallization in hydrated silica-rich melts: empirical models of plagioclase nucleation and growth kinetics. J. Petrol. 53, 1743–1766.

Mourtada-Bonnefoi, C., Laporte, D., 1999. Experimental study of homogeneous bubble nucleation in rhyolitic magmas. Geophys. Res. Lett. 26, 3505–3508.

Mourtada-Bonnefoi, C., Laporte, D., 2004. Kinetics of bubble nucleation in a rhyolitic melt: an experimental study of the effect of ascent rate. Earth Planet. Sci. Lett. 218, 521–537.

Mueller, S., Melnik, O., Spieler, O., Scheu, B., Dingwell, D.B., 2005. Permeability and degassing of dome lavas undergoing rapid decompression: an experimental determination. Bull. Volcanol. 67, 526–538.

Navon, O., Chekhmir, A., Lyakhovsky, V., 1998. Bubble growth in highly viscous melts: theory, experiments, and autoexplosivity of dome lavas. Earth Planet. Sci. Lett. 160, 763–776.

Okumura, S., Nakamura, M., Nakano, T., Uesugi, K., Tsuchiyama, A., 2012. Experimental constraints on permeable gas transport in crystalline silicic magmas. Contrib. Mineral. Petrol. 164, 493–504.

Okumura, S., Nakamura, M., Takeuchi, S., Tsuchiyama, A., Nakano, S., Uesugi, K., 2009. Magma deformation may induce non-explosive volcanism via degassing through bubble networks. Earth Planet. Sci. Lett. 281, 267–274.

Okumura, S., Nakamura, M., Uesugi, K., Nakano, T., Fujioka, T., 2013. Coupled effect of magma degassing and rheology on silicic volcanism. Earth Planet. Sci. Lett. 362, 163–170.

Polacci, M., Papale, P., Rosi, M., 2001. Textural heterogeneities in pumices from climactic eruption of Mount Pinatubo, 15 June 1991, and implications for magma ascent dynamics. Bull. Volcanol. 63, 83–97.

Proussevitch, A.A., Sahagian, D.L., 1996. Dynamics of coupled diffusive and compressive bubble growth in magmatic systems. J. Geophys. Res. 101 (B8), 17447–17455.

Proussevitch, A.A., Sahagian, D.L., 1998. Dynamics and energetics of bubble growth in magmas: analytical formulation and numerical modeling. J. Geophys. Res. 103 (B8), 18223–18251.
Rust, A.C., Cashman, K.V., 2004. Permeability of vesicular silicic magma: inertial and hysteresis effects. Earth Planet. Sci. Lett. 228, 93–107.
Rust, A.C., Manga, M., 2002. Effects of bubble deformation on the viscosity of dilute suspensions. J. Non-Newton. Fluid Mech. 104, 53–63.
Rutherford, M.J., Gardner, J.E., 2000. Rates of magma ascent. In: Sigurdsson, H. (Ed.), Encyclopedia of Volcanoes. Academic San Diego, California, pp. 207–217.
Sahimi, M., 1994. Applications of Percolation Theory. Taylor and Francis, London, 258 pp.
Saul, A., Wagner, W., 1989. A fundamental equation for water covering the range from the melting line to 1273 K at pressures up to 25 000 MPa. J. Phys. Chem. 18 (4), 1537–1565.
Scaillet, B., Evans, B.W., 1999. The 15 June 1991 eruption of Mount Pinatubo. I. Phase equilibria and pre-eruption $P–T–fO_2–fH_2O$ conditions of the dacite magma. J. Petrol. 40, 381–411.
Sparks, R.S.J., 1978. The dynamics of bubble formation and growth in magmas: a review and analysis. J. Volcanol. Geotherm. Res. 3, 1–37.
Sparks, R.S.J., 1997. Causes and consequences of pressurisation in lava dome eruptions. Earth Planet. Sci. Lett. 150, 177–189.
Takeuchi, S., Tomiya, A., Shinohara, H., 2009. Degassing conditions for permeable silicic magmas: implications from decompression experiments with constant rates. Earth Planet. Sci. Lett. 283, 101–110.
Toramaru, A., 1989. Vesiculation process and bubble size distributions in ascending magmas with constant velocities. J. Geophys. Res. 94 (B12), 17523–17542.
Toramaru, A., 1995. Numerical study of nucleation and growth of bubbles in viscous magmas. J. Geophys. Res. 100 (B2), 1913–1931.
Toramaru, A., 2006. BND (bubble number density) decompression rate meter for explosive volcanic eruptions. J. Volcanol. Geotherm. Res. 154, 303–316.
Toramaru, A., 2014. On the second nucleation of bubbles in magmas under sudden decompression. Earth Planet. Sci. Lett. 404, 190–199.
Westrich, H.R., Eichelberger, J.C., 1994. Gas transport and bubble collapse in rhyolitic magma: an experimental approach. Bull. Volcanol. 56, 447–458.
Wolfe, E.W., Hoblitt, R.P., 1996. Overview of the eruptions. In: Newhall, C.G., Punongbayan, R.S. (Eds.), Fire and Mud: Eruptions and Lahars of Mount Pinatubo. University of Washington Press, Seattle, pp. 3–20.
Wright, H.M.N., Cashman, K.V., Gottesfeld, E.H., Roberts, J.J., 2009. Pore structure of volcanic clasts: measurements of permeability and electrical conductivity. Earth Planet. Sci. Lett. 280, 93–104.
Zhang, Y., Behrens, H., 2000. H_2O diffusion in rhyolitic melts and glasses. Chem. Geol. 169, 243–262.